Nanotechnology 29.35 (2018): 355707

DOI: http://dx.doi.org/10.1088/1361-6528/aacb91

Size-selective breaking of the core-shell structure of gallium nanoparticles

S. Catalán-Gómez[1]*, A. Redondo-Cubero[1], F.J. Palomares[2], L. Vázquez[2], E. Nogales[3], F. Nucciarelli[1,4], B. Méndez[3], N. Gordillo[1], and J.L. Pau[1]

[1]*Grupo de Electrónica y Semiconductores, Departamento de Física Aplicada, Universidad Autónoma de Madrid, Cantoblanco, E-28049 Madrid (Spain).*

[2] *Instituto de Ciencia de Materiales de Madrid, CSIC, Cantoblanco, E-28049 Madrid (Spain).*

[3]*Facultad de Ciencias Físicas, Departamento de Física de Materiales, Universidad Complutense de Madrid, E-28040 Madrid (Spain).*

[4]*Physics Department, Lancaster University, Lancaster LA1 4YB (United Kingdom).*

Corresponding author: sergio.catalan@uam.es

Abstract

Core-shell gallium nanoparticles (Ga NPs) have recently been proposed as an ultraviolet plasmonic material for different applications but only at room temperature. Here, the thermal stability as a function of the size of the NPs is reported over a wide range of temperatures. We analyse the chemical and structural properties of the oxide shell by x-ray photoelectron spectroscopy and atomic force microscopy. We demonstrate the inverse dependence of the shell breaking temperature with the size of the NPs. Spectroscopic ellipsometry is used for tracking the rupture and its mechanism is systematically investigated by scanning electron microscopy, grazing incidence x-ray diffraction and cathodoluminescence. Taking advantage of the thermal stability of the NPs, we perform complete oxidations that lead to homogenous gallium oxide NPs. Thus, this study set the physical limits of Ga NPs to last at high temperatures, and opens up the possibility to achieve totally oxidized NPs while keeping their sphericity.

1. Introduction

Metallic nanoparticles (NPs) have been, for a long time, the focus of the research community due to their unique electrical, optical, catalytic and sensing properties[1]. One of their most studied properties is their capability to confine the light thanks to the excitation of their free electrons (plasmons)[2]. This confinement arises from a localized surface plasmon resonance (LSPR) that occurs at a characteristic frequency of each material and strongly depends on the surrounding media[3].

As a metallic material, gallium (Ga) has its bulk plasma frequency in the ultraviolet (UV) range (14 eV)[4]. In the form of NPs, the plasmon resonance can, however, be varied in a wide spectral range from the UV to the infrared depending on their size and shape[5]. Ga NPs typically exhibit hemispherical shape by self-assembly when grown on different substrates such as polymers, glass, fused silica, sapphire, graphite or silicon (Si). The two different axes cause two different resonances: the out-of-plane resonance (shortest axis) at higher energies and the in-plane resonance (largest axis) at lower energies[6].

One of the advantages of using Ga NPs is that they can be produced in a simple, fast and cost effective manner using thermal evaporation at low temperatures. During the deposition, Ga NPs merge due to coalescence or coarsening processes, sometimes ascribed to the Ostwald ripening mechanism[7].

After the deposition, when NPs are exposed to air, a native gallium oxide (Ga_2O_3) is formed around the liquid Ga that preserves it in a supercooled state and is amorphous[8]. This passivating layer has a self-limiting thickness between 0.5-3 nm due to the attenuation of oxygen diffusion[9,10].

Despite the formation of the native oxide layer, this core-shell structure has exhibited good properties in different applications such as surface-enhanced Raman scattering[11,12], solid-liquid phase change memories[13], waveguiding[14] and ellipsometric biosensing[15,16].

Although the native oxide plays a key role in the liquid core-oxide shell stability, little attention has been paid to it so far. In a previous work, we studied the role of this oxide in the chemical functionalization of the Ga NPs[17]. In particular, we found out that the formation of thiol-based self-assembly monolayer can be better identified when the oxide thickness is enlarged by thermal treatments providing better NPs stability. Moreover, the

oxidation at low temperatures was demonstrated to be an accurate approach to tune the plasmon resonance wavelength of the NPs[18].

In this work we study the mechanical and compositional properties of the oxide shell in a large temperature range, from room temperature (RT) up to 900 ºC, at atmospheric pressure. The rupture mechanism of the oxide shell is analysed by different morphological, optical and structural techniques. We determine the breaking temperature of the NPs as a function of their size, and we analyse the changes in their plasmonic properties.

2. Experimental

Ga NPs are deposited by Joule-effect thermal evaporation using a vertical Edwards E306 system operating in high vacuum conditions (base pressure of 2×10^{-7} mbar). The size of the NPs depends on the total amount of Ga in the evaporation crucible. Different masses have been evaporated in order to obtain different NP mean radius. In particular, we deposited 30, 75, 120, 260, 340 and 410 mg of Ga mass. A 99.9999% purity Ga was used for the evaporation processes. These have been carried out under 50 W power, applied to a tungsten filament (99.90% purity). The working pressure during deposition was 1.5×10^{-5} mbar. Si (100) substrates were placed 200 mm away from the Ga source. The substrate holder is ice-cooled to avoid surface migration and coalescence of the NPs by unintentional heating.

Thermal treatments of the NPs were performed at atmospheric pressure in a horizontal quartz tube connected to a gas supply line with a QuadraTherm mass flow meter. The temperature inside the furnace is monitored by a proportional-integral-derivative controller. For the oxidation, a constant flow of 80 standard cubic centimetres (sccm) of 99.999% pure O_2 was used. Two factors were varied during the oxidation processes, either the temperature up to 900 ºC or the oxidation time up to 1200 min. After the oxidation process, the samples were extracted from the tube, cooling down in ambient conditions.

The optical properties of the samples were analysed by spectroscopic ellipsometry (SE), using a Jobin Yvon UVISEL system equipped with a Xe lamp (1.5-4.5 eV energy range), a 0º modulator and a 45º analyser. The measurements are taken in external reflection configuration at 70º incidence angle referred to the normal of the sample surface. The

pseudo-dielectric constants of the material were obtained from the ellipsometric parameters psi (ψ) and delta (Δ)[19].

Scanning electron microscopy (SEM) was used to study the morphology of the Ga NPs. The microscope is a FEI XL30-SFEG system, operating with 10 keV electron beam and nominal lateral resolution of 4 nm, being the secondary electrons collected and analysed with an Everhart-Thornley detector.

The crystal structure of the samples has been analysed by grazing incidence X-ray diffraction (GIXRD) using a X'Pert Pro Panalytical system. The incident beam is produced in a Cu X-ray tube, focused by a Göbel mirror and collimated in a Soller slit (0.04 rad). The diffracted beam passes through a 0.18º parallel plate collimator, a graphite (002) monochromator, and a Soller slit (0.04 rad) before being detected with a Xe gas scintillator. The incident angle was fixed at 0.5º and the 2θ angle was varied from 10º up to 90º, with a step of 0.04º and an acquisition time of 4 s per point.

X-ray photoelectron spectroscopy (XPS) has been used to characterize the chemical composition of Ga NPs deposited on Si wafer substrates. XPS spectra were acquired in an UHV chamber with a base pressure of 10^{-10} mbar equipped with a hemispherical electron energy analyser (SPECS Phoibos 150 spectrometer) and a 2-D delay-line detector, using a monochromatic Al-K_α (1486.74 eV) X-ray source. High-resolution spectra were recorded at normal emission using an energy step of 0.025 eV and a pass-energy of 10 eV, which provide an overall instrumental peak broadening of 0.45 eV. The absolute binding energies of the photoelectron spectra were determined by referencing to the Si $2p_{3/2}$ transition at 99.0 eV. The spectra were analysed with the program XPSPEAK41 using a Shirley method for background subtraction.

Atomic Force Microscopy (AFM) served us as a technique for the morphological characterization of the NPs. Si cantilevers whose tips have a nominal radius of 8 nm and force constant of 40 N/m (Brucker) were employed for the topographical measurements in an Agilent PicoPlus 5500 system, operating in dinamic mode. Images were analysed and post-processed with Gwyddion program[20]. Kelvin probe force microscopy (KPFM) was also analysed in the same setup in order to measure the surface potential across the samples. For these measurements, platinum-coated cantilevers with a nominal force constant of 3.5 N/m and radius of 20 nm (©µmasch) were employed. KPFM measures the contact Potential Difference (CPD), which is the difference in the work function values of the imaged sample location and that of the tip[21].

Chatodoluminescence (CL) measurements were performed in order to characterize the optical properties of the samples after an oxidation process. The CL detector collects the signal generated within a Leica Stereoscan 440 SEM microscope. All the measurements were taken with a voltage and beam current of 20 kV and 2 nA respectively. Energy Dispersive X-ray Spectroscopy was also performed with a Bruker detector whitin the same system. The voltage was set to 20 keV and the insensity was increased to 15 nA.

3. Results

3.1 Low temperature regime

After the deposition, the initial structure of Ga NPs is a liquid metallic core surrounded by a native gallium oxide shell. The latter is formed after exposing NPs to ambient air. Fig. 1 (a) shows a sketch of this typical core-shell structure on a Si substrate. This sketch corresponds well with the morphological characterization performed on the NPs. Fig. 1(c) shows a bimodal distribution of NPs obtained after evaporating 340 mg of Ga. In addition to the topographical image (AFM image), the KPFM inset was used to characterize the surface potential, since this technique is sensitive to changes in the chemical composition and thickness variation, among others[21]. It can be seen that the CPD signal is quite uniform and does not appreciably change for the different NPs displayed, which indicates that the native oxide is uniform.

During the thermal oxidation process, part of the liquid metallic Ga is oxidized and forms the gallium oxide shell. After the quenching, the remaining liquid Ga experiences a volume reduction that results in a deformation of the shell and the formation of dips, as we discussed extensively in our previous work[18]. This is shown in the sketch of Fig. 1 (b), which reflects the morphology found for the samples oxidized under 300ºC during 15 minutes, displayed in Fig. 1 (d) where the dips are marked with dashed squares. The existence of dips suggests that the shell has elastic properties to accommodate to the liquid Ga core after quenching. As a matter of fact, the KPFM inset in Fig. 1 (d) reveals the existence of a clear spatial contrast in the CPD signal on top of each NP. This contrast is ascribed to local changes in the oxide thickness of the shell or in its stoichiometry.

The histogram from the as-deposited sample is shown in Fig. 1 (e) where the second mode has a average NP radius of 138 nm. This mode will have more importance than the smaller one as explained later on.

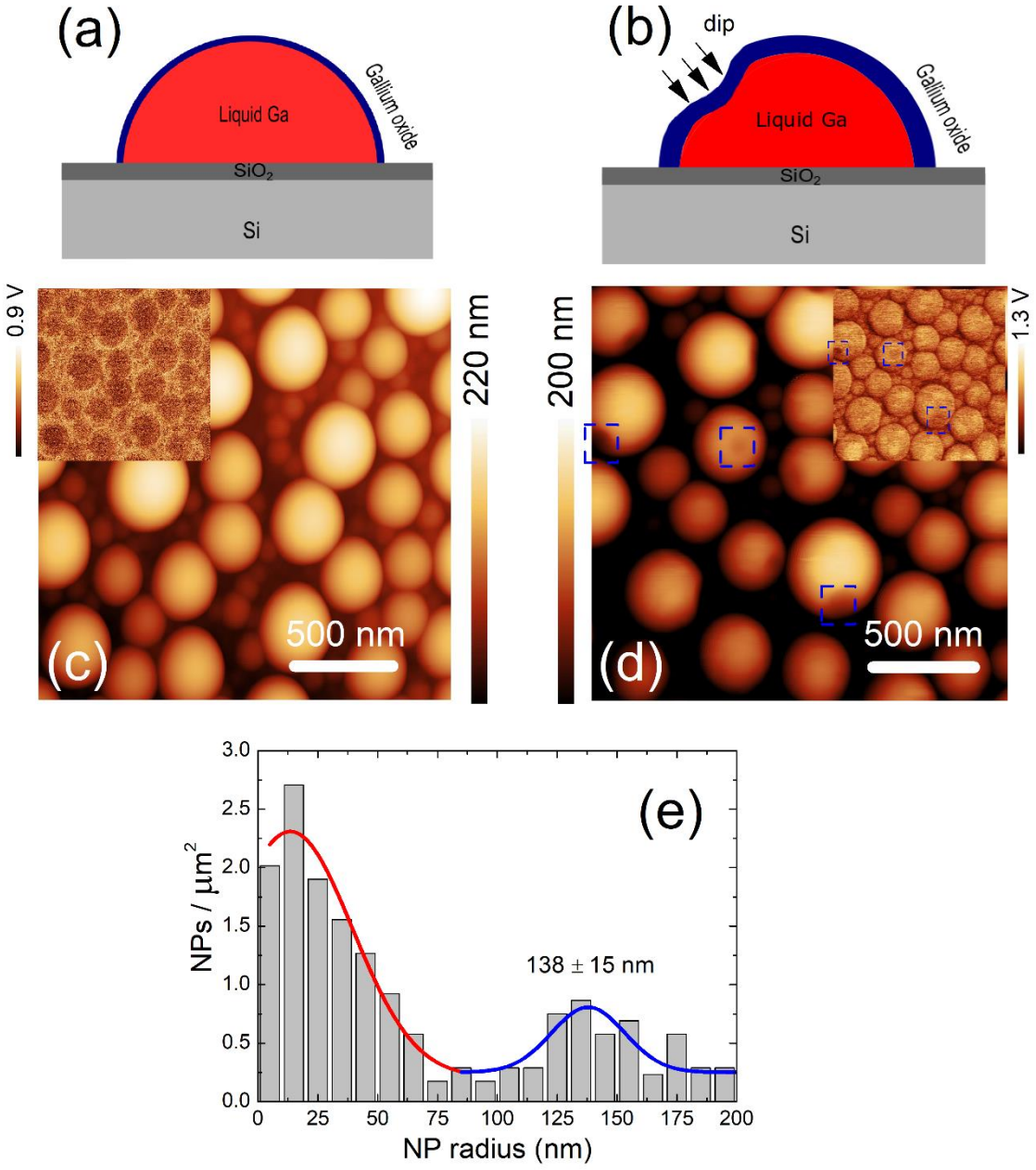

Figure 1. Skecth of an isolated NP on a SiO_2-Si substrate of the a) as-deposited sample and b) 300 ºC oxidized sample. AFM images of the a) as-deposited sample and b) 300 ºC oxidized sample. The location of the different dips are marked by dashed squares in d). The insets correspond to the simultaneous KPFM images taken on the same area. The vertical scales correspond to the contact potential difference signal. d) Histogram of the size distribution of the as-deposited sample with the corresponding gaussian fits.

We have carried out X-ray photoelectron spectroscopy (XPS) measurements in order to chemically study the core-shell structure before and after thermal oxidation. The Ga 3d level has a escape depth of photoelectrons around 8 nm[22] that is sufficient to detect the core signal since the native oxide is 1-3 nm length. The XPS analysis of the as-deposited

sample (black solid line) is shown in Fig. 2 (a). The two peaks at low binding energies correspond to the doublet of metallic Ga while the other main peak around 21 eV is ascribed to the gallium oxide signal as reported in literature[23]. This doublet comes from the Ga oxidation state of +3 and its position is in agreement with the measurement of the reference sample of Ga_2O_3[18]. O 2s broad peak is found at higher binding energies (~24 eV). The spectra cannot be fitted with only four gaussian-lorentzian (60%) functions, since a high χ^2~6 is obtained. Thus, we propose two additional doublets for the fit, which would suggest the presence of suboxides within the oxide shell. The fit of the as-deposited sample is plotted below its experimental curve in Fig. 2 (a). For the fit, the area ratio has been constrained to be 2/3 for peaks from doublets and the FWHM of each doublet has been maintained constant, which increases with the oxidation state. The value of the spin-orbit splitting was also limited to 0.45 eV for all doublets. An asymmetry factor of 0.077 has been added to the gaussian-lorentzian function of the metallic Ga as described in literature[24] according to the Doniach-Sunjic theory. Doublets 5/2 and 3/2 are indicated in the figure with solid and dashed line, respectively. The first suboxide (blue color) that would correspond to the oxidation state of +1 is placed around 19.1 eV with a FWHM of 0.72 eV and the second suboxide (orange color) around 20.2 eV with a FWHM of 0.99 eV attributed to an oxidation state +2. The metallic doublet is placed around 18.5 eV with a FWHM of 0.47 eV and the oxide 3+ at 21.1 eV with a FWHM of 1.2 eV. Although lower oxidation states of Ga are less stable than the Ga^{+3}, some groups have found evidences of GaO and Ga_2O in thin films of GaAs[22,25-27]. The spectrum with these four additional functions (2 doublets) is well fitted giving a χ^2 of 0.34. The area ratio of each doublet over the whole fitted area is shown in Table 1. Although the metallic and oxide 3+ doublets play the main role, the oxide 1+ and 2+ are required for an adequate fit.

We have analysed the same sample under a higher electron emission angle in order to have a lower sampling depth, i.e., maximizing the signal from the oxide shell and, correspondingly, minimizing the metallic signal from the core. Fig. 2 (a) shows the comparison between 0º (normal emission) and 60º take-off measurements (red dashed line). Despite the higher angle, the low binding energy region increases, which cannot be assigned to a higher metallic signal since the sampling depth is reduced. Thus, it should be explained by a higher emission from de oxide 1+ (Ga_2O), which evidences again the presence of this suboxide. The need of the oxide 2+ component is clearly seen to account

for the intensity increase of the valley on the region around 20 eV where this oxide 2+ is located.

Regarding the physical origin of these suboxides, the interfaces are commonly recognized as places for formation of low oxidation states due to the presence of broken or unsaturated bonds. In our case, in the lowest interface, core Ga-shell Ga_xO_y, the solid oxide shell must accommodate itself onto the liquid metal likely provoking the formation of suboxides in addition to the growth of the stoichiometric and more stable oxide (Ga_2O_3). In addition, there exist dangling bonds, defects and hydroxides in the outmost oxide shell interface that cause the formation/presence of lower oxidations states.

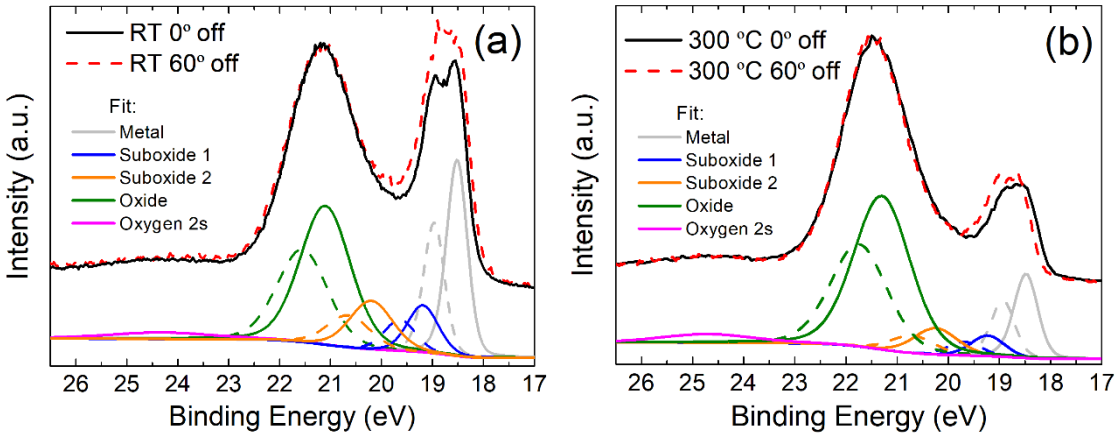

Figure 2. (a) XPS spectra of the 3d level of Ga for the as-deposited sample with a fit of a Ga metallic doublet, 3 Ga-O different doublets and a oxygen singlet. Suboxide 1,2 and oxide refers to Ga_2O, GaO and Ga_2O_3, respectively. The experimental spectra of the 60º take-off is also presented. (b) Same scenario than (a) but for the sample oxidized at 300 ºC.

Once the as-deposited sample has been studied, we have analysed the sample oxidized at 300 ºC for 15 min (solid black line of Fig. 2 (b)). Clearly, the signal from the low binding energy region decreases compared to the as-deposited sample (Fig. 2 (a)) as a consequence of the oxide growth, whose thickness increases around 4-5 nm as estimated in our previous work[18]. The fit is presented below the experimental curve. The area ratio of each doublet in this case is also presented in Table 1. It can be seen how the area ratio of the Ga 3+ contributes more to the total area in the 300º C oxidized sample than in the as-deposited one. Furthermore, the area ratio of the other low states (1+, 2+) doublets decreases upon thermal oxidation, which suggests the formation of an better quality oxide in terms of stoichiometry since the main contribution comes from its highest oxidation state, +3. In adittion, the Fig. 2 (b) shows the 60º take-off measurement of the 300 ºC

oxidized sample. In this case, the doublet metallic region does not increase compared to its 0º take off counterpart. At 300 ºC, the atoms from the thermally grown oxide would have enough energy to accommodate in their more stable oxidation state. Consequently, the oxide shell is likely more stoichiometric.

Table 1. Data from the fit of the XPS measurement of the as-deposited sample corresponding with a 3d metallic doublet and three 3d oxides doublets.

Peak	Area ratio for as-deposited 0º off (%)	Area ratio for 300 ºC oxidized 0º off (%)
Metal	27.89	15.96
Suboxide 1 (Ga_2O)	9.59	5.28
Suboxide 2 (GaO)	13.84	8.76
Oxide (Ga_2O_3)	45.77	66.3

3.2 High temperature regime

Our annealing processes at high temperatures lead to the rupture of the gallium oxide shell[18]. This rupture, however, depends on the size of the NPs. In order to characterize and determine the breaking temperature we carried out experiments with four samples with different NP sizes, obtained after the deposition of 30, 75, 120 and 340 mg of Ga, respectively. Oxidation time was maintained constant and equal to 15 min for the whole set of samples. After oxidations, a detailed SEM characterization was done in each sample in order to evaluate the shell integrity around the NP. The shell breakdown can be easily identified by SEM, since the inner liquid is ejected from the core, as shown later.

Fig. 3 shows the SEM images of the sample of 75 mg of Ga mass (average radius of 30 nm) oxidized for 15 min at 600 ºC (a) and 700 ºC (b) , respectively. While the NPs remain undamaged at 600 ºC, the NPs after 700 ºC annealing have lost their sphericity and show grains on top. These facts are compatible with the formation of a polycristalline oxide layer, later on confirmed by the GIXRD, and, therefore, evidencing the breaking of the shell and the ejection of liquid Ga outwards. Accordingly, we identify the rupture temperature in this sample to be 650±50 ºC. Fig. 3 (c) shows the results of the breaking temperature as a function of Ga NP radius (and Ga mass) for the whole set of samples. The radius in the *x* axis is obtained from the average NP radius of the second mode of the

histogram, which is tipically bimodal as shown in Fig. 1 (e). The reason to take in account the second mode and not the average of the histogram is because the biggest NPs break earlier in terms of temperature than the smallest ones. The results confirm that small NPs are more stable upon annealing than bigger ones.

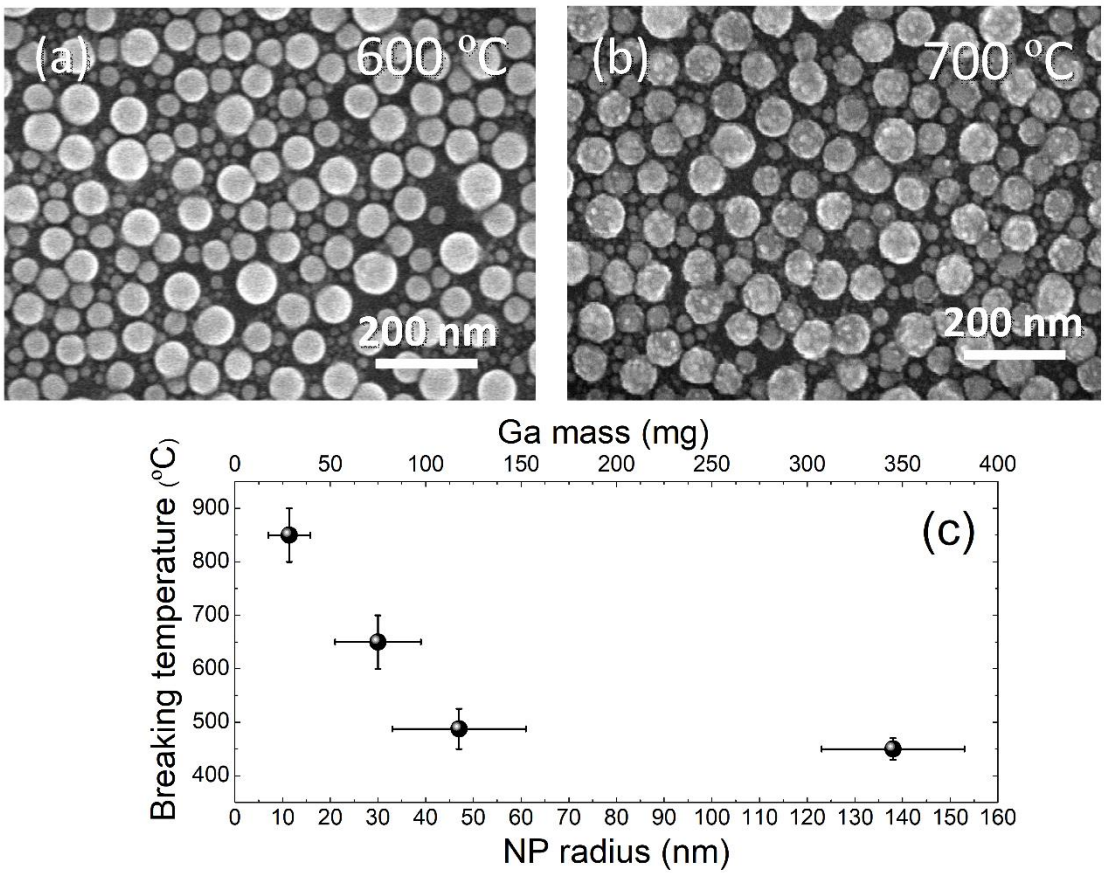

Figure 3. SEM image of the sample with NP radius of 30 nm oxidized during 15 min at a) 600 ºC and b) 700 ºC. c) Core-shell breaking temperature as a function of the NP radius and Ga mass.

In adittion to the SEM characterization, the SE spectra of all the samples can also be used to track the transformation of the NPs. Figure 4 (a) shows the LSPR in-plane mode of the sample with the lowest average radius (11 nm). The resonance is located around 400 nm for the as-deposited sample. As the temperature is increased, the LSPR intensity only undergoes a slight atenuation until 800 ºC. At 900 ºC, the associated absorption band dissapears due to the breakdown of the shell, also verified by SEM (not shown). Interestingly, the transformation of the NPs can be also achieved for a fixed temperature if the oxidation time is increased orders of magnitude. Figure 4 (b) represents the evolution of the in-plane resonance for different oxidation times at 700 ºC. This temperature is sufficiently high to boost the diffusion but it is far from the breaking

temperature (850 ºC) in order to avoid the shell rupture. In this case, the LSPR shows, again, a slight attenuattion with oxidation time up to 600 min when the resonance is vanished. Despite the lack of LSPR, the SEM characterization shows no rupture of the core-shell NPs (image not shown). These arguments suggest that the NPs are totally oxidized at 700 ºC for 600 min. It is worth noticing that the total transformation to gallium oxide can only be achieved with the smallest NPs since they remain unbroken for long times at higher temperatures.

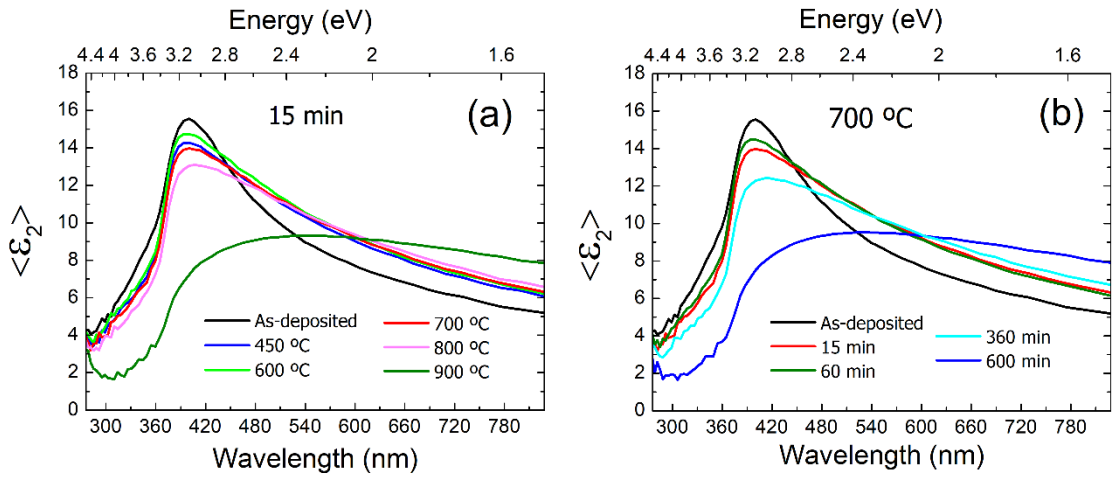

Figure 4. a) SE measurements of the sample with NP average radius of 11 nm oxidized at a) different temperatures for15 min b) different times at 700 ºC.

Fig. 5 shows the SEM images of the NPs with biggest size for temperatures: 450ºC (a), 600ºC (b) and 900ºC (c). The corresponding as-deposited NPs were already shown in Fig. 1 (b). In all the cases (above 450ºC), the shell is broken. The rupture of the shell can be explained by different factors. On the one hand, the elevated temperature increase from RT to 450 ºC produces an increment of the vapour pressure of liquid Ga from 10^{-8} to 10^{-4} torr[28]. On the other hand, it should be taken into account the two orders of magnitude difference in the thermal expansion coefficient between liquid gallium and gallium oxide[29]. Theoretically, a temperature change about 400 ºC would lead to a volume increase of a 5% of the liquid gallium according to the formula $\Delta V/V_0=\alpha\cdot\Delta T$. In contrast, the change in the Ga_2O_3 shell can be neglected (0.2%). Gallium oxide constrains the expansion of the core and this stress is released causing a fissure and provoking the shell breakdown. The liquid gallium is thermally expanded and ejected from the shell following a volcano-like behaviour (Fig. 5 (a)). When the liquid gallium makes contact with the O_2 flow in the furnace, it is oxidized and forms an irregular shape onto the NP surface (Fig. 5 (b)). As the temperature increases, less liquid Ga would remain in the core.

In addition, above 800-900 ºC nanowires may grow from the surface of the NPs[30] as marked in the Fig. 5 (c) with dashed squares. The sketch of Fig. 5 (d) illustrates the breakdown of the NPs and the ejection from the core.

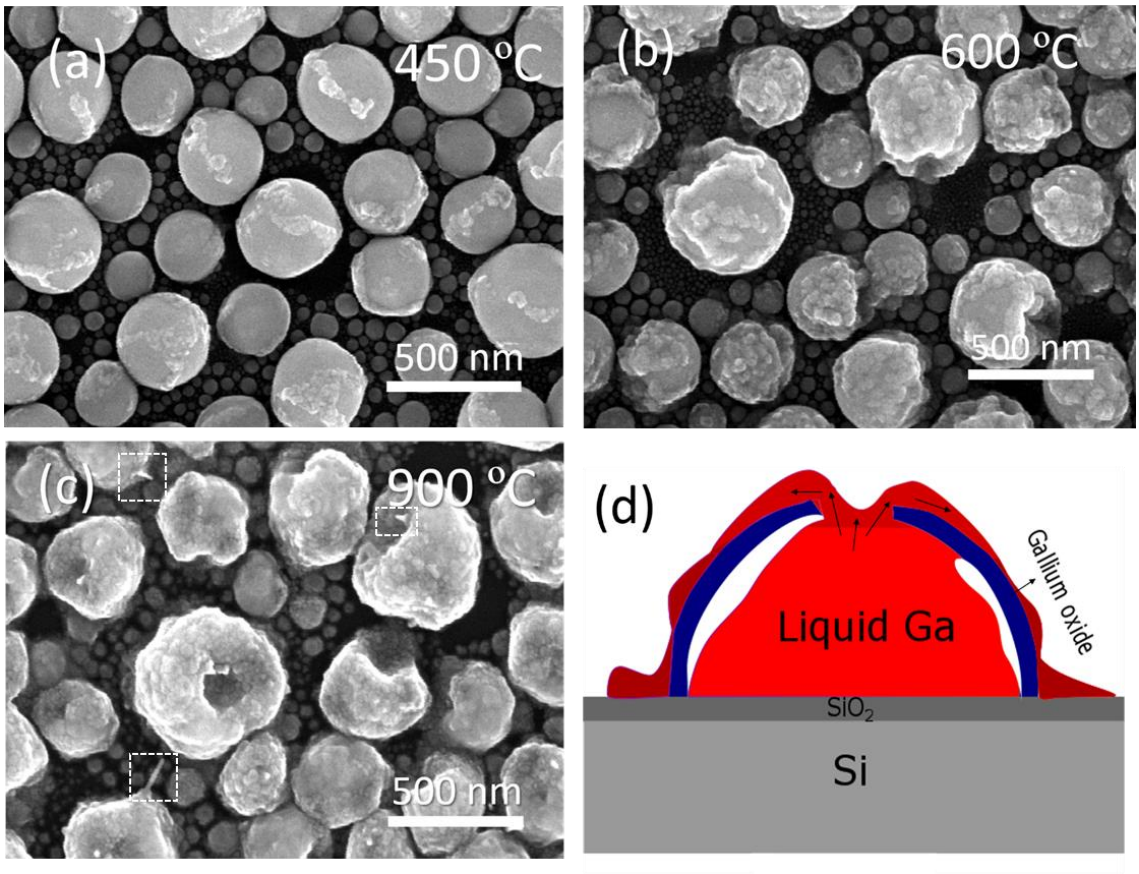

Figure 5. SEM image of the sample with 340 mg of Ga oxidized at a) 450 ºC, b) 600 ºC and c) 900 ºC. d) Sketch of the rupture mechanism with a volcano-like behavior.

Grazing Incidence X-Ray Diffraction (GIXRD) measurements were performed in order to figure out the crystallinity after the thermal processes. Fig. 6 (a) shows how the double band ascribed to liquid Ga[8] decreased from RT to 300 ºC due to transformation of liquid Ga into Ga_2O_3. When temperature keeps increasing, narrow peaks appear related to polycrystalline growth. These peaks fit the crystal lattice of the β-Ga_2O_3 indicated in the figure. The formation of the oxide is promoted by the fact that in the phase diagram Ga-O, very low concentration of O_2 is needed for the formation of β-Ga_2O_3. In addition, O_2 has high solubility in liquid Ga[31]. The peak intensity of the direction (002) is higher for 900 ºC probably evidencing the nanowires crystal growth along the "z" axis.

Additional cathodoluminiscence (CL) and energy dispersive X-ray spectroscopy (EDX) measurements of the NPs are shown in Fig. 6 (b), revealing the typical violet-blue

emission band of defects caused by bound excitons and donor–acceptor pairs (DAP) transitions[32]. The intensity of the band is highly increased with the oxidation temperature and so it is the gallium oxide concentration. It is important to note that before the rupture (<450 ºC for this NP radius), no CL band was found. The ratio between the EDX Ga-L peak intensity and O-K one decreases with the annealing temperature (inset in Fig. 6 (b)), indicating an incorporation of oxygen atoms to the samples. There is a strong kink of the ratio when the shell breaks down at about 450 ºC, in agreement with the breakdown of the NPs and the ejection of the liquid Ga and the exposure to the O gas. The absence of any other peaks in the EDX spectrum apart from Ga and O evidences that no other element interfere in this process.

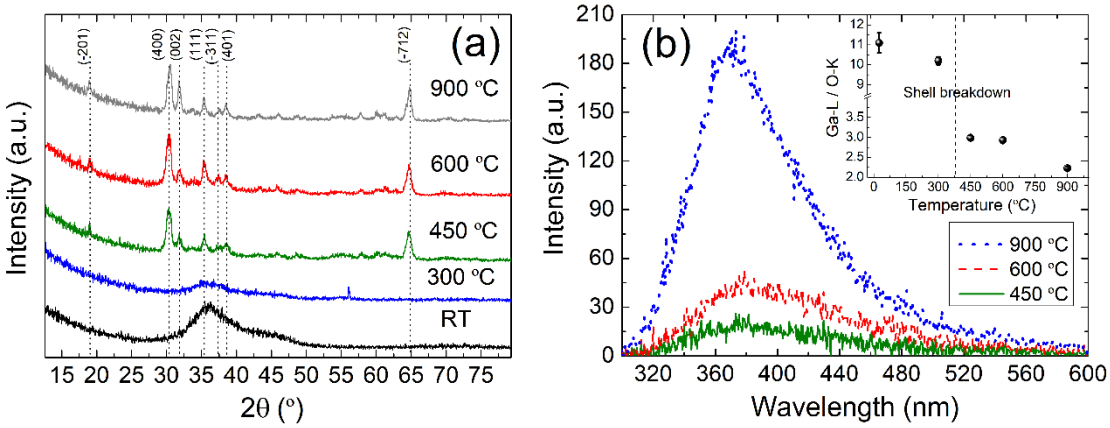

Figure 6. a) GIXRD measurements of the 340 mg of Ga samples oxidized at different temperatures. Dot points indicate the crystal lattice of β-Ga_2O_3. b) CL measurements of the same samples. The inset represents de EDX measurements with the Ga-L peak intensity over O-K peak intensity as a function of the annealing temperature.

All these results reveal how the core-shell structure of the NPs behaves with temperature. The mechanisms discussed in detail for the mass of 340 mg (Fig. 5), suggesting that Ga is ejected due to the increase of the inner pressure at high temperatures, can be also assumed for other Ga masses. Thus, the main difference arises from the particle size since the smallest NPs remain unbroken. The thermal stability of the small Ga NPs (with diameters below 30 nm) has been demonstrated to be up to 850 ºC, which opens up the possibility to work at high temperatures without significance reduction of the plasmon resonance intensity.

From a practical point of view, a higher thermal stability outspreads oxidation processes at higher temperatures, what means a higher diffusion and higher tunability of the

plasmon resonance by gallium oxide growth. Regarding the applications for sensing, the relevant plasmonic mode is the out-of-plane one[16]. Thus, in the following, we focus our study on the oxidation of the NPs with a detectable out-of-plane mode in the optical range of the SE. Indeed, the plasmon resonance wavelength redshifts only for the out-of-plane mode and not for the in-plane mode as it is shown in Fig. 4. This fact has also been demonstrated with Finite-Difference Time-Domain simulations by other authors[33]. In order to study how the plasmon tunability changes with temperature, samples with NPs around 138 nm of radius (340 mg of Ga) have been oxidized for different times at temperatures of 200, 300 and 400 ºC. Fig. 7 (a) shows the redshift as a function of time. The graph shows that a maximum redshift (tunability), denoted with $\Delta\lambda$, of 11 ± 2 nm can be achieved at 200 ºC while for 300 ºC, the maximum plasmon resonance wavelength can be redshift up to 62 ± 2 nm. This value is higher at 300 ºC because the process is thermally activated as it was demonstrated with an Arrenhius-like behaviour in our previous work[18]. In the 400 ºC case, only oxidations up to 30 min can be done. After that time, oxide shell breaks and the plasmon resonance signal is vanished. The arrow in the graph indicates the oxidation time limit before the rupture. In this scenario, the temperature (400ºC) is too close to the rupture temperature (450 ºC) shown in Fig. 3 (a).

Taking advantage of the higher thermal stability (Fig. 3 (a)) and with the aim to improve the tunability range, we have carried out thermal oxidations at 400 ºC for different times for samples with a lower NP radius (47 ± 2 and 92 ± 3 nm approximately) and a sample with a higher NP radius (180 ± 6 nm). The SE measurements are presented in Fig. 7 (b). A $\Delta\lambda$ value of 113 nm is obtained after an oxidation for 100 min of a sample with a mean NP radius of 47 nm (black spheres). In the case of bigger NPs, the gallium oxide shell breaks earlier and the maximum redshifted is reduced. In particular, samples with NP radius of 92 (red stars) and 180 nm (blue squares) shows a maximum $\Delta\lambda$ of 47 and 50 nm, respectively. Those values are much lower than 113 nm, which demonstrates that a reduction of the NP size implies not only an improvement of the thermal stability but also a broader range of plasmon tunability.

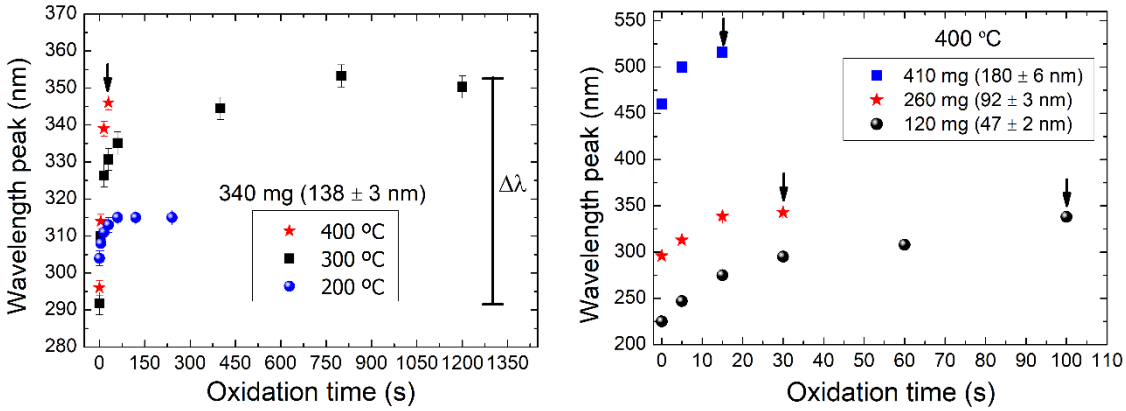

Figure 7. a) Maximum plasmon resonance wavelength by SE as a function of oxidation time for the sample of 340 mg oxidized at different temperatures. b) Same plot with samples of different NP radius oxidized at a fixed temperature of 400 ºC.

Since for NPs with radius below 47 nm the out-of-plane mode is located at higher energies in the UV, out of our SE spectral range, the tracking cannot be done for those cases.

Thus, the transition between liquid Ga core to gallium oxide can be achieved by changing the oxidation time. This helps to tune the effective permittivity of the NP layer, which can have potential application as a coating layer for the optimization of optoelectronic devices.

4. Conclusions

In summary, we have studied the thermal stability of the core-shell structure of Ga NPs over a wide range of temperatures and NP radius. With the XPS results, we have been able to demonstrate the presence of different oxidation states in the native oxide of the Ga NPs core-shell interface, which was never reported for the system of metallic Ga NPs. Moreover, we have observed a strong dependence of the shell breaking temperature with NP size. We have estimated that the smallest NPs keep unbroken up to 850 ºC. Furthermore, the shell rupture threshold was analysed by a rigorous characterization with SEM, XRD and CL. Finally, we have considered different advantages of the improved thermal stability in the smallest NPs such as a higher LSPR tunability and a total oxidation of the liquid Ga into Ga_2O_3 while preserving the morphology integrity of the NPs. Our results provide an easy and effective method to control the liquid Ga-Ga_2O_3 ratio by thermal treatments and give an insight for the use of plasmonic Ga NPs at high temperatures.

Acknowledgments

We thank Eduardo Ruiz for technical help during the sample preparation. The research is supported by the MINECO (CTQ2014-53334-C2-2-R, CTQ2017-84309-C2-2-R, MAT2016-80394-R, MAT 2015-65274-R/FEDER and MAT2017-85089-C2-1-R) and Comunidad de Madrid (NANOAVANSENS ref. S2013/MIT-3029) projects. ARC acknowledges Ramón y Cajal program (under contract number RYC-2015-18047). FN acknowledges support from Marie Sklodowska-Curie grant agreement No 641899 from the European Union´s Horizon 2020 research and innovation programme.

References

1 Mody, V. V., Siwale, R., Singh, A. & Mody, H. R. 2010 Introduction to metallic nanoparticles *J. Pharm. Bioallied Sci.* **2** 282-289.

2 García, M. A. 2012 Surface plasmons in metallic nanoparticles: fundamentals and applications *J. Appl. Phys.* **45**

3 Stockman, M. I. 2011 Nanoplasmonics: past, present, and glimpse into future *Opt. Express* **19** 22029-22106.

4 Hunderi, O. & Ryberg, R. 1974 Band structure and optical properties of gallium *J. Phys. F: Metal Phys.* **4** 2084.

5 Albella, P. *et al.* 2011 Shape Matters: Plasmonic Nanoparticle Shape Enhances Interaction with Dielectric Substrate *Nano Lett.* **11** 3531-3537.

6 Wu, P. C. *et al.* 2007 Real-time plasmon resonance tuning of liquid Ga nanoparticles by in situ spectroscopic ellipsometry *Appl. Phys. Lett.* **90** 103119.

7 Woorhees, P. W. 1985 Theory of Ostwald Ripening *J. Stat. Phys.* **38**

8 Yarema, M. *et al.* 2014 Monodisperse Colloidal Gallium Nanoparticles: Synthesis, Low Temperature Crystallization, Surface Plasmon Resonance and Li-Ion Storage *J. Am. Chem. Soc.* **136** 12422-12430.

9 Sanz, J. M. *et al.* 2013 UV Plasmonic Behavior of Various Metal Nanoparticles in the Near- and Far-Field Regimes: Geometry and Substrate Effects *J. Phys. Chem. C* **117** 19606-19615.

10 Wipakorn, J. *et al.* 2014 Self-limiting growth of ultrathin Ga_2O_3 for the passivation of Al2O3 /InGaAs interfaces *Appl. Phys. Express* **7** 011201.

11 Wu, P. C. *et al.* 2009 Demonstration of Surface-Enhanced Raman Scattering by Tunable, Plasmonic Gallium Nanoparticles *J. Am. Chem. Soc.* **131** 12032-12033.

12 Yang, Y., Callahan, J. M., Kim, T.-H., Brown, A. S. & Everitt, H. O. 2013 Ultraviolet Nanoplasmonics: A Demonstration of Surface-Enhanced Raman Spectroscopy, Fluorescence, and Photodegradation Using Gallium Nanoparticles *Nano Lett.* **13** 2837-2841.

13 Soares, B. F., Jonsson, F. & Zheludev, N. I. 2007 All-optical phase-change memory in a single gallium nanoparticle *Phys. Rev. Lett.* **98**

14 Krasavin, A. V. & Zheludev, N. I. 2004 Active plasmonics: Controlling signals in Au/Ga waveguide using nanoscale structural transformations *Appl. Phys. Lett.* **84** 1416-1418.

15 Antonio, G. M. *et al.* 2015 Immunosensing platform based on gallium nanoparticle arrays on silicon substrates *Biosens. Bioelectron.* **74** 1069-1075.

16 Antonio, G. M. *et al.* 2016 Gallium plasmonic nanoparticles for label-free DNA and single nucleotide polymorphism sensing *Nanoscale* **8** 9842-9851.

17 Catalán-Gómez, S. *et al.* The role of the oxide shell in the chemical functionalization of plasmonic gallium nanoparticles in *SPIE Optics + Optoelectronics.* **10231** 2017.
18 Catalán-Gómez, S., Redondo-Cubero, A., Palomares, F. J., Nucciarelli, F. & Pau, J. L. 2017 Tunable plasmonic resonance of gallium nanoparticles by thermal oxidation at low temperatures *Nanotechnology* **28** 405705.
19 Tompkins, H. G. in *A User's Guide to Ellipsometry* 1-18 (Academic Press, 1993).
20 Nečas, D. & Klapetek, P. 2012 Gwyddion: an open-source software for SPM data analysis *Open Phys.* **10** 181-188.
21 Sadewasser, S. & Glatzel, T. 2012 *Kelvin Probe Force Microscopy* (Berlin:Springer).
22 Surdu-Bob, C. C., Saied, S. O. & Sullivan, J. L. 2001 An X-ray photoelectron spectroscopy study of the oxides of GaAs *Appl. Surf. Sci.* **183** 126-136.
23 Carli, R. & Bianchi, C. L. 1994 XPS analysis of gallium oxides *Appl. Surf. Sci.* **74** 99-102.
24 Widstrand, S. M. *et al.* 2014 Core-Level Photoemission From Stoichiometric GaN(0001)-1×1 *MRS Internet J. Nitride Semicond. Res.* **10** e1.
25 Gocalinska, A., Rubini, S. & Pelucchi, E. 2016 Native oxides formation and surface wettability of epitaxial III–V materials: The case of InP and GaAs *Appl. Surf. Sci.* **383** 19-27.
26 Ballutaud, D., Debiemme-Chouvy, C., Etcheberry, A., de Mierry, P. & Svob, L. 1995 Reactivity of III–V and II–VI semiconductors toward hydrogen: surface modification and evolution in air *Appl. Surf. Sci.* **84** 187-192.
27 Palomares, F. J. *et al.* 2001 Electron-beam-induced reactions at O_2/GaAs(100) interfaces *Surf. Sci.* **482-485** 121-127.
28 Richard, E. H. & Dean, A. K. 1969 *Vapor Pressure Data for the Solid and Liquid Elements* RCA Laboratories.
29 Víllora, E. G., Shimamura, K., Ujiie, T. & Aoki, K. 2008 Electrical conductivity and lattice expansion of β-Ga2O3 below room temperature *Appl. Phys. Lett.* **92** 202118.
30 Prokes, S. M., Carlos, W. E. & Glembocki, O. J. Growth and characterization of single crystal Ga_2O_3 nanowires and nano-ribbons for sensing applications in *Proceedings of the SPIE.* **6008** 2005.
31 Zinkevich, M. & Aldinger, F. 2004 Thermodynamic Assessment of the Gallium-Oxygen System *J. Am. Ceram. Soc.* **87** 683-691.
32 Alonso-Orts, M. *et al.* 2017 Shape Engineering Driven by Selective Growth of SnO_2 on Doped Ga_2O_3 Nanowires *Nano Lett.* **17** 515-522.
33 Knight, M. W. *et al.* 2015 Gallium Plasmonics: Deep Subwavelength Spectroscopic Imaging of Single and Interacting Gallium Nanoparticles *ACS Nano* **9** 2049-2060.